Magnetic Regulation of Thermo-Chemotherapy from a Cucurbit[7]uril-Crosslinked Hybrid Hydrogel [*]

*Haishi Qiao, Jing Jia, Wei Chen, Bin Di, Oren A. Scherman, Chi Hu** [†]

Introduction

The development of thermal therapies is an important component of cancer therapeutics today as (1) they are associated with fewer side effects in comparison to chemo- and radiotherapies; (2) they can reach deep-seated and poorly-accessible tumors; and (3) they can be used in combination with all conventional treatment modalities.[1–3] Hyperthermia (the heating of cancer tissues to between 41 and 45 °C) and thermoablation (the heating of tumors to above 50 °C to induce cell necrosis) have both been proven to potentially improve the efficacy of cancer therapy by either directly killing tumor cells or making the cells more susceptible to concomitant chemotherapy.[4,5] Now, thermal therapy is primarily used for clinical treatment of small, unresectable tumors for patients who are in poor surgical conditions.[6] Iron oxide nanoparticles, magnetite Fe_3O_4 and maghemite γ-Fe_2O_3, are widely used for thermal therapy on account of their biocompatibility and that their metabolic pathways are known.[7,8] Since 1957, they have been directly injected into tumor tissue where they are stimulated by an alternating magnetic field ($\vec{B}$) to produce heat arising from Brownian and Néel relaxation processes.[9] Despite the promising results, thermal therapy has not widely been established in clinical routines, as the following major challenges still hinder its practicability: (1) restriction of local heating to the tumor site without damaging surrounding tissue, and (2) generation of thermal effects without using invasive heating probes.[10–12]

[*] This research has been supported by the Natural Science Foundation of Jiangsu Province (SBK2017041610), the National Natural Science Foundation of China (NSFC 81600178 and 81803485).

[†] Dr. H. Qiao, Prof. W. Chen, Prof. C. Hu
Department of Pharmaceutical Engineering
China Pharmaceutical University
Nanjing, 210009 (China)
E-mail: chihu@cpu.edu.cn
J. Jia, Prof. B. Di
Key Laboratory of Drug Quality Control and Pharmacovigilance
China Pharmaceutical University
Nanjing, 210009 (China)
Prof. O. A. Scherman
Melville Laboratory for Polymer Synthesis
Department of Chemistry, University of Cambridge
Cambridge, CB2 1EW (UK)

Supporting information for this article is available on the WWW under http://www.your.website.com or from the author.

Chitosan (CS), a natural component of shrimp and crab shells, is a cationic polysaccharide with amino functional groups, which has become prominent in biomedical applications on account of its biocompatible and biodegradable properties.[13–15] Examples of its use in the formation of hydrogels have shown good promise in applications such as 3D cell culture scaffolds and injectable drug delivery depots.[16,17] Nanoparticle-encapsulated hybrid hydrogels based on CS have also been developed in recent reports in order to optimize their therapeutic efficiency. While some systems prepared *via* simply mixing the polymer backbone of CS with the incorporated nanoparticles suffer from lack of internal interactions between the two species, others employ covalent reactions to facilitate such internal bonding within the material.[18,19] In the latter case, however, decoration with crosslinkable derivatives and the subsequent covalent reaction hamper stability of the nanoparticles, resulting in compromised physical and chemical properties.

Cucurbit[7]uril (CB[7]) belongs to a family of barrel-shaped macrocyclic host molecules, cucurbit[*n*]urils (CB[*n*]s), which exhibit unique structural and molecular recognition properties.[20,21] A variety of "guest" molecules such as cyclic and aromatic compounds are able to bind inside CB[7] in aqueous systems, making it a suitable molecular receptor for biomedical applications.[22] Confined by its size, CB[7] typically accommodates only one guest molecule inside its cavity at a given time.[23,24] CB[7] has recently been employed as a linking motif to prepare supramolecular hydrogels,[25,26] nanoparticles,[27,28] functional surfaces,[29] etc. Tan and coworkers have reported CB[7]-adamantane crosslinked supramolecular hydrogels and demonstrated a method to control their gelation kinetics by using competing guest molecules.[30] Kuhn *et al.* presented the electrokinetic assembly of 1D gold-nanoparticle chains with fixed and rigid CB[7]-nanojunctions of 9 *Å*.[31] Little attention, however, has been focused on the development of hybrid supramolecular hydrogel (HSH) with incorporated nanoparticles using CB[7] as a non-covalent linker to enhance interactions between the two species.

Herein, we report a supramolecular method to obtain robust non-covalent interactions between a hydrogel matrix and nanoparticles incorporated within the polymer network, where a self-assembly process was employed rather than direct chemical modification on the nanoparticle surfaces. As shown schematically in Figure 1, CB[7] was

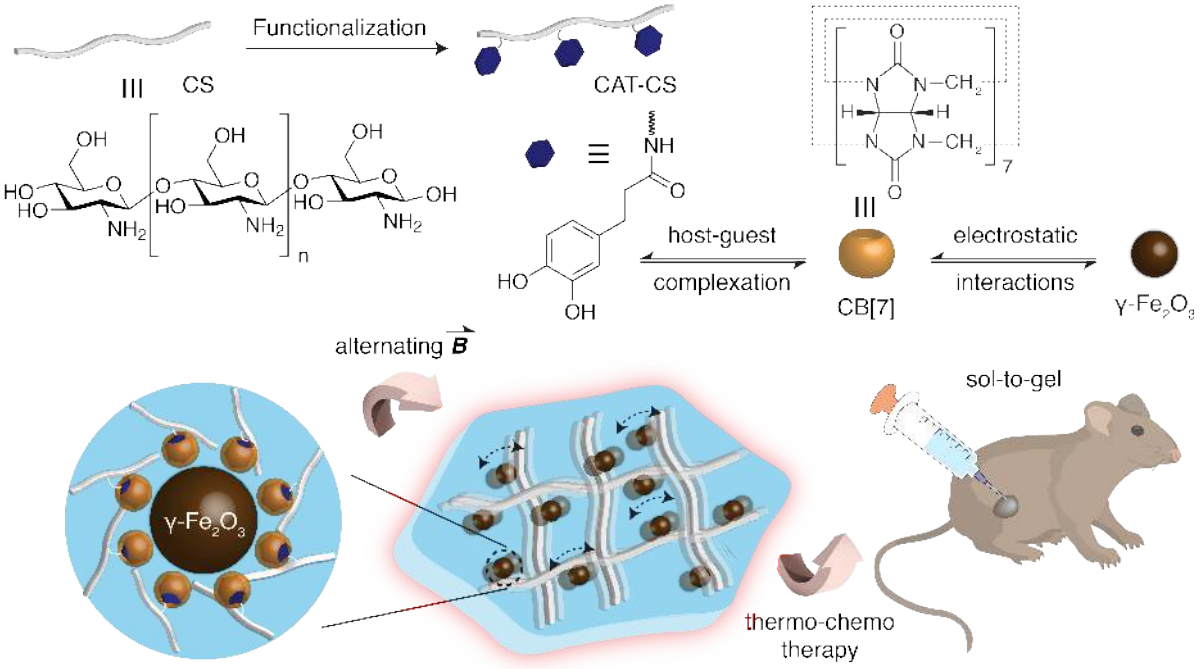

Figure 1. Schematic illustration of magnetic hydrogel nanocomposite prepared *via* CB[7]-mediated molecular recognition and electrostatic interactions.

employed as a non-covalent linker to facilitate interactions between catechol-functionalized chitosan (CAT-CS) and superparamagnetic γ-Fe_2O_3 nanoparticles. Multivalent side-chain functional polymer CAT-CS bearing catechol derivatives, which forms a thermoresponsive hydrogel upon addition of glycerophosphate (GP), was synthesized *via* post-functionalization of the natural polysaccharide chitosan.[32] The CAT functional groups could be readily recognized and encapsulated by CB[7], while the carbonyl portals of CB[7] bind with γ-Fe_2O_3 nanoparticles through electrostatic interactions, giving rise to a noncovalent-bonded network between the polymer backbone and the nanoparticles.[33–36] The prepared HSH will be fixed in place due to the compression of surrounding tissues after local injection. Increased drug release kinetics and local heating to the tumor site could be achieved at the same time under $\vec{B}$, as vibration of the γ-Fe_2O_3 nanoparticles attached non-covalently to CS creates a continuous movement of the polymer backbone.[37,38]

Results and Discussion

CAT-CS (2 wt%) was firstly solubilized in acidic conditions *via* protonation of its amino groups, and its pH was increased to a physiologically acceptable neutral range upon addition of GP due to the neutralization effect of the phosphate groups (base), leading to the formation of a hydrogel-like precipitate.[39–41] Addition of GP transforms the purely pH-dependent CS solution to a temperature-controlled pH-dependent mixture, which remains liquid at physiological pH and turns into a hydrogel if heated to body temperature, making the system an ideal candidate as an injectable biomaterial.[42,43] An approach to prepare thermally sensitive hydrogels based on CS/GP combinations was demonstrated by Chenite and coworkers, and the formed system was used to deliver growth factors *in vivo* as well as to encapsulate living chondrocytes for tissue engineering applications.[44]

Complexation with one equivalent of CB[7] was achieved *via* sonication, and the formation of binary complexes CAT⊂CB[7] on the polymer side-chains was confirmed by NMR studies, where CAT signals show broadening and upfield shift upon complexation with CB[7] (Figure 2A). Figure 2B displays the isothermal titration calorimetry (ITC) data for the titration of CAT-CS into a buffered solution of CB[7] and shows an isotherm that fits well to an independent sites model, showing an inflection point at the 1:1 molar ratio of CAT to CB[7] with a binding constant of 2.97×10^5 M^{-1}. The presence of the inflection point at perfect 1:1 stoichiometry verifies that all CAT units on the polymer backbone are accessible and take part in the complexation with CB[7]. Superparamagnetic γ-Fe_2O_3 nanoparticles with an average diameter of 7 nm as obtained from TEM imaging and an average hydrodynamic diameter of 29 nm as calculated by dynamic light scattering (DLS) were added (0.1 wt%), and the assembled HSH was studied for its rheological properties during a heating-cooling cycle. As shown in Figure 2C, HSH demonstrates a sharp rise in storage modulus (G') upon heating, indicating that the liquid solution turned into a solid-like gel in the vicinity of 37 °C.

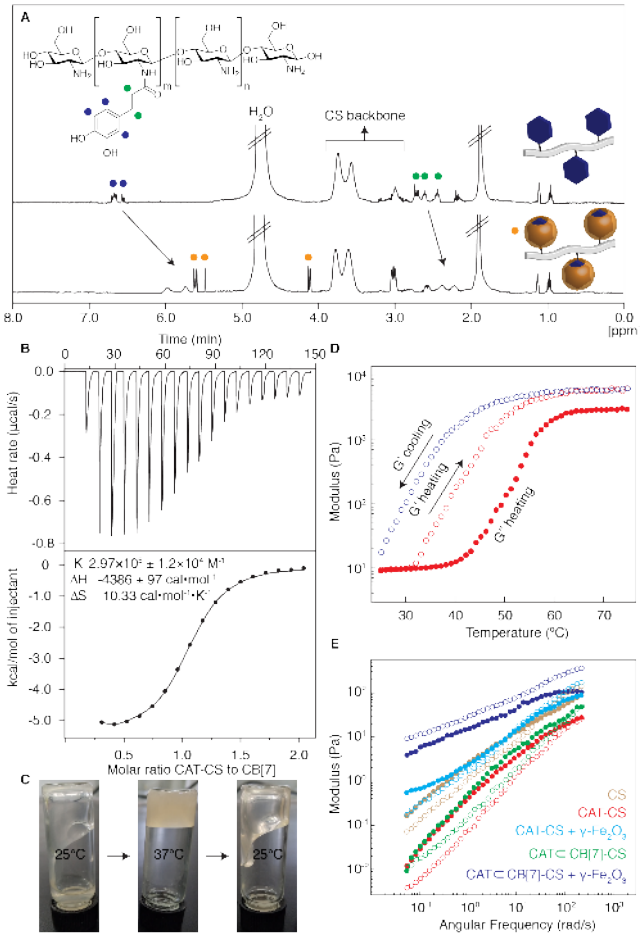

Figure 2. (A) ^{1}HNMR spectra of (top) CAT-CS and (bottom) CAT⊂CB[7]-CS in D_2O. Signals for CAT functional groups show broadening and upfield shift upon complexation with CB[7], as denoted by the arrows. (B) Stoichiometry and thermodynamic parameters for the binding of CAT-CS to CB[7], as determined by ITC employing an independent sites model. CAT-CS ([CAT] = 1 mM) was titrated into a solution of CB[7] (0.1 mM, 950 μL) in 10 mM PBS buffer at pH 7.4. The top plot displays the power applied as a function of time, and the bottom plot displays integrated enthalpy values as a function of the molar ratio of CAT functional groups titrated into CB[7]. The binding stoichiometry was determined to be 1:1 and the binding constant to be 2.97×10^5 M^{-1}. (C) Sol/gel transition and (D) inverted vial test of the HSH containing 2 wt% CAT-CS and 0.1 wt% γ-Fe_2O_3 nanoparticles during a heating-cooling cycle at 1 °C min^{-1} from 25 to 75 °C. The crossover between storage modulus G' and loss modulus G" represents the start of the hydrogel formation. (E) Steady shear measurements at 37 °C of hydrogels prepared with and without CB[7] as a crosslinking agent.

This is consistent with visual observation where HSH remains liquid under room temperature but exhibits a quick sol-to-gel conversion when heated to body temperature, giving rise to potential applications as an injectable delivery system (Figure 2D). The decrease in G' during cooling reveals a propensity of the gel to return to a liquid state. Compared with the loss modulus (G"), which also increases upon heating, G' dominates throughout the temperature sweep, suggesting that the hydrogel is a structured material with persistent internal interactions. It is noteworthy that pure γ-Fe_2O_3 nanoparticles tend to agglomerate into larger structures, which dramatically influence their biomedical and magnetic properties. Induced coordination through the CB[7] carbonyl portals could effectively protect and stabilize the nanoparticles to form a homogeneous dispersion within HSH.

As shown in Figure 2E, the gradients expressed by CAT-CS and CAT⊂CB[7]-CS hydrogels are slightly steeper and more frequency dependent compared to those of the CS material, indicating a weaker internal structure with a greater degree of reordering of the system at low frequencies. Also the functionalization of CS with CAT units moves the stress relaxation point (crossover of G' and G") to higher frequencies, likely because the EDC coupling reaction lowers the percentage of amine groups on the polymer backbone of CS, decreasing the interactions between the polymer chains and GP during the hydrogel formation process. On the contrary, HSH with encapsulated nanoparticles exhibits a much stronger internal network than CS, CAT-CS and CAT⊂CB[7]-CS materials, exemplified by G' > G" throughout the frequency sweep and the relatively steady gradients, *i.e.*, the system is more static and less dependent on applied frequency. It is noteworthy that CAT-CS with incorporated γ-Fe_2O_3 nanoparticles also shows enhanced modulus in comparison to the native CAT-CS hydrogel, which is likely on account of the formation of coordination bonding between catechol derivatives and the nanoparticles. This enhancement, however, is not as strong as that of the HSH, suggesting that CAT⊂CB[7]-CS is bonded to the γ-Fe_2O_3 nanoparticles through CB[7] instead of the CAT groups. The difference in rheological behaviors between hydrogels with or without incorporated nanoparticles indicates non-covalent bonding between γ-Fe_2O_3 nanoparticles and the polymer chain, which together form a robust coordination-crosslinked network.

The prepared HSH exhibits two featured properties upon exposure to $\vec{B}$, (1) an accelerated drug release rate as the non-covalent network vibrates together with the superparamagnetic γ-Fe_2O_3 nanoparticles, and (2) an increased temperature for thermal treatment. Doxorubicin (Dox), a model therapeutic, was encapsulated into the HSH at room temperature in order to study its controlled release properties. Dox-loaded HSH (disc diameter 12.5 mm, height 5 mm, [Dox] = 30 μM) was placed in complete growth medium (3 ml) and exposed to $\vec{B}$ for different length of time to induce vibration and heating within the material. Dox was well retained within the HSH upon its sol-to-gel transition, and the release of Dox into the surrounding system was monitored using ultraviolet-visible (UV-Vis) spectroscopy, where the concentration of Dox was determined by fitting its normalized absorbance to the calibration curve. As shown by the square symbols in Figure 3A, an initial burst release of Dox was observed when the HSH was irradiated under $\vec{B}$, followed by a plateau stage where the release slows down significantly. After exposure to $\vec{B}$ for 12 min, only 33% of

loaded Dox was released, indicating that sustained release could be achieved using HSH as a drug carrier.

In comparison with the efficient Dox release demonstrated by the HSH, samples prepared without employing CB[7] to introduce non-covalent interactions between the nanoparticles and the polymer backbone showed slower release rates with a final release of only 14% after irradiation under $\vec{B}$ for 12 min, which is much lower than the value obtained using the HSH assembled in the presence of CB[7] (triangles in Figure 3A). This phenomenon confirms the important role of CB[7] as a non-covalent linker in the assembly of HSH, which possesses an integrated network with robust internal interactions. A control experiment was conducted without the application of $\vec{B}$, and no measurable release after 12 min was observed as shown by the cross symbols in Figure 3A, supporting our hypothesis that the release kinetics was accelerated through the vibration of γ-Fe_2O_3 nanoparticles under $\vec{B}$.

The thermal response of the HSH was investigated by irradiating it under $\vec{B}$ for different lengths of time. As shown in Figure 3B, the HSH was heated upon exposure to magnetic field, where a dramatic increase in temperature was observed in the first 3 min followed by gradual heating between 3 to 6 min and a subsequent plateau. The heating effect is dependent on the nanoparticle loading (0, 0.05, 0.1, 0.15 and 0.2 wt%), and higher concentrations of γ-Fe_2O_3 nanoparticles clearly give rise to greater changes in temperature. The HSH with 0.1% nanoparticles shows a final temperature increase of approx. 35 °C, which is suitable for thermal treatment and was chosen for the rest of the study.

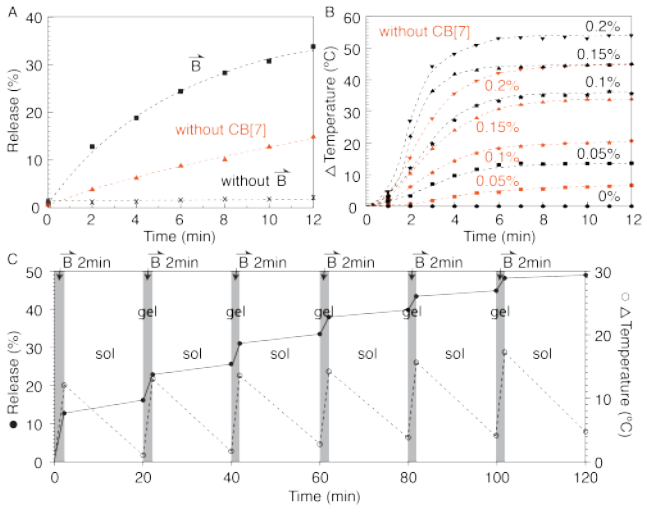

Figure 3. Responses of the HSH to an alternating magnetic field. (A) Release of loaded Dox as a function of the irradiation time under $\vec{B}$. (B) Temperature increase in HSHs prepared with different concentrations of γ-Fe_2O_3 nanoparticles. (C) Drug-release and temperature-increase profiles of Dox-loaded HSH during six cycles of $\vec{B}$ irradiation. In each cycle, samples were treated in the presence of $\vec{B}$ for 2 min and in the absence of $\vec{B}$ for 18 min.

Moreover, the HSH was exposed to six cycles of $\vec{B}$ irradiation, where in each cycle the material was treated in the presence of magnetic field for 2 min and in the absence of magnetic field for 18 min. As shown in Figure 3C, accelerated drug release was observed under $\vec{B}$ in each cycle on account of the oscillation of magnetic nanoparticles, which induces the coordination-bonded network to vibrate. It is noteworthy that while the remarkable heating effects related to Néel and Brown losses during the magnetization reversal process of γ-Fe_2O_3 nanoparticles subjected to $\vec{B}$ increase temperature of the sample and maintain the material in its gel form, the HSH undergoes a gel-to-sol conversion and readily flows under room temperature. Thus the HSH relaxes and cools down in the absence of $\vec{B}$ in each cycle as denoted by the dashed lines in Figure 3C, resulting in a gel-to-sol conversion which also facilitates drug release as polymers in the sol state attribute less preservation to the loaded cargo. The cargo release kinetics in the absence of $\vec{B}$, however, is much slower compared to that under $\vec{B}$ irradiation, inferring that dynamic oscillation of the hydrogel network is more efficient in triggering drug release compared to static diffusion from the sol state hydrogel. The final release reaches 49% of overall loaded Dox after six cycles of alternating $\vec{B}$ and natural conditions.

The ability of the HSH to facilitate thermal therapy as well as controlled drug release is demonstrated *in vitro* with HeLa cells, where these two properties are examined separately in parallel in order to compare their efficiency. For heat treatment, the HSH (γ-Fe_2O_3 nanoparticles = 0.1%) was placed *under* the cell culture dish and exposed to $\vec{B}$ for 12 min. Cells were then returned to the incubator and cultured for 24 h, allowing time for a cellular response before being stained with Annexin V-FITC/PI for apoptosis analysis. As shown in Figure 4A, the proportion of early apoptotic cells (d: Annexin V-FITC$^+$/PI$^-$) and late apoptotic/necrotic cells (b: Annexin V-FITC$^+$/PI$^+$) reaches 39.1% after thermal treatment for 12 min. Fluorescence assay was performed using Calcein-AM (green) and PI (red) costaining to differentiate live and dead cells after treatment. As shown in Figure 4B, both live (green) and dead (red) cells were found in the fluorescence microscopy image, and slightly more live cells present than the dead ones. This observation is consistent with the results from flow cytometry, suggesting that exposure to $\vec{B}$ induces tumor cell apoptosis through increasing the temperature.

For *in vitro* study of its drug delivery ability, Dox-loaded HSH was soaked in complete growth medium and exposed to $\vec{B}$ for 12 min. The growth medium was aspirated from the HSH and used to cultivate HeLa cells for 24 h before testing. As shown in Figure 4C, the proportion of apoptotic cells reaches 65.7% as measured by flow cytometry, and this value is also validated by the fluorescence microscopy image in Figure 4D, where the number of dead cells is slightly higher than that of viable cells. In the control group, Dox-loaded HSH was soaked in complete growth medium for 12 min in

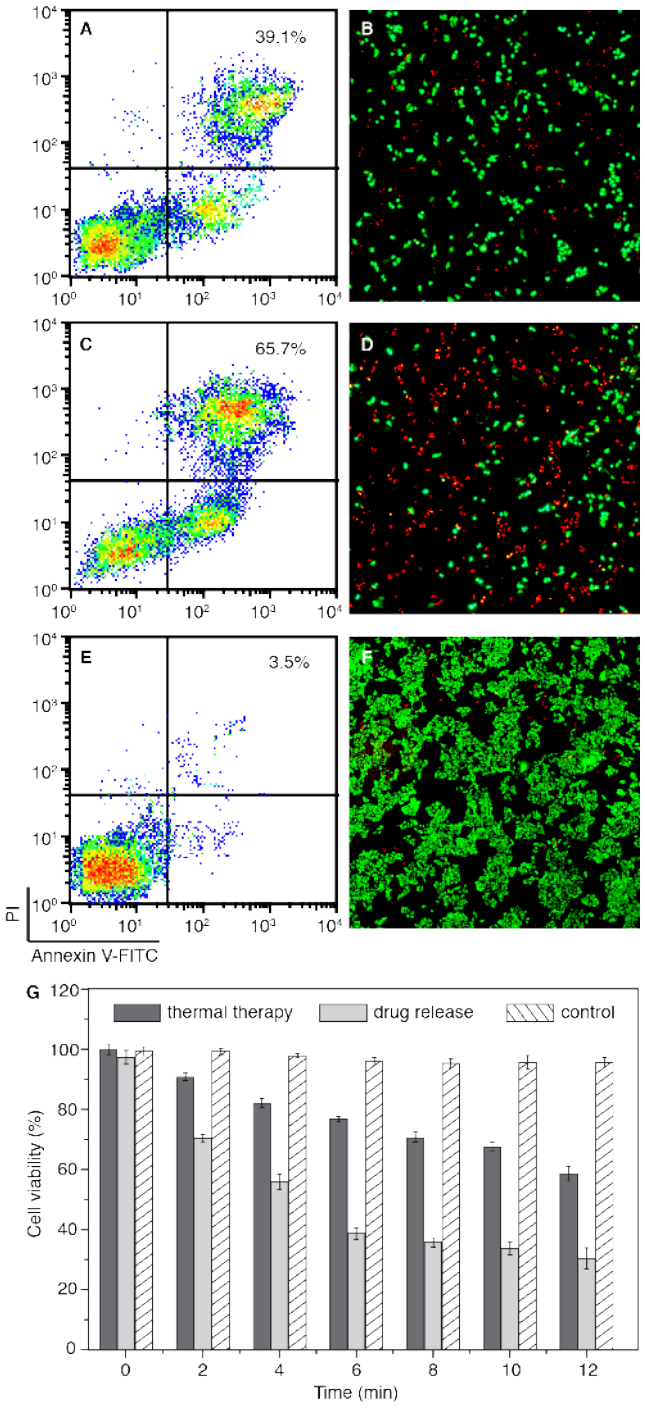

Figure 4. *In vitro* cell studies using HSH as a platform for thermo-chemotherapy. Efficiency of thermal treatment (A, B), drug release (C, D) and control experiment (E, F) was presented in HeLa cells. Cells were stained with Annexin V-FITC/PI for flow cytometry analysis (A, C, E), Calcein-AM/PI for fluorescent microscopy imaging (B, D, F), and MTT for cell viability calculation (G).

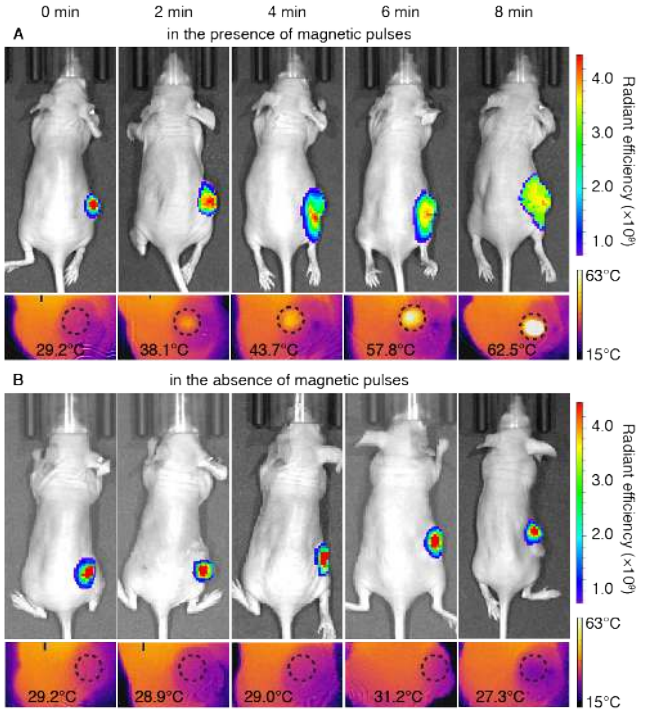

Figure 5. Intravital fluorescence imaging and infrared thermography of tumor-bearing nude mice injected with ICG-loaded HSH in the presence (A) and in the absence (B) of $\vec{B}$ for different length of time.

the absence of $\vec{B}$, and the growth medium was aspirated from the HSH and used to cultivate HeLa cells for 24 h before testing. Apoptotic cells comprise only 3.5% as calculated by flow cytometry in Figure 4E, and dead cells are almost negligible in the fluorescence microscopy image in Figure 4F, indicating that drug release from the HSH is accelerated only in the presence of $\vec{B}$.

In order to confirm the reliance of thermal therapy and drug release on the external stimulus, cell viability was tested by MTT assay under various exposure time to $\vec{B}$. As shown in Figure 4G, cell viability decreases significantly with prolonged exposure to $\vec{B}$ (from 0 to 12 min) for both thermal therapy and drug release, however, the latter exhibits a more pronounced effect with a final value of approx. 30% after irradiation under $\vec{B}$ for 12 min. A control experiment was conducted without $\vec{B}$ and the cell viability was almost 100%, confirming biocompatibility of the HSH.[45,46]

Based on the favorable results of the *in vitro* cell studies, the HSH was formulated with indocyanine green (ICG) as a model cargo to investigate its *in vivo* release characteristics. ICG-loaded HSH was injected directly into the tumors on adult BALB/c nude mice and the release was monitored *via* intravital fluorescence imaging (Figure 5). A consistent release pattern was observed where ICG reached more area of the tumor tissue with prolonged exposure to $\vec{B}$ (Figure 5A). On the contrary, control experiments where mice were treated in the absence of $\vec{B}$ did not show release of ICG within the same time frame examined, indicating that cargo release was governed by the applied magnetic field, which

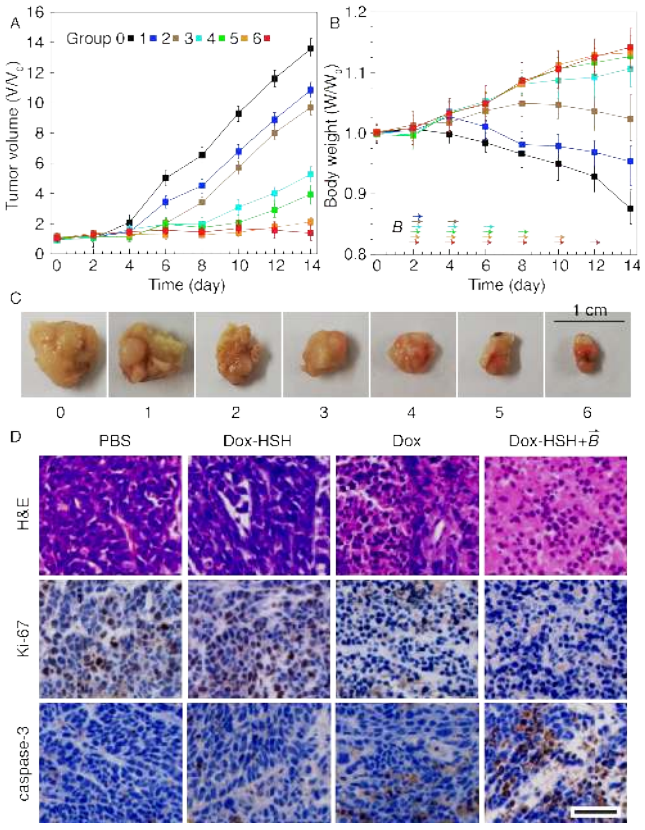

Figure 6. Thermo-chemotherapy mediated by magnetic field diminishes xenograft tumor growth in mice. Changes in tumor volume (A) and body weight (B) within 14 days of treatment, with arrows indicating the time when $\vec{B}$ was applied. Images of tumors explanted at the end of the study (C). Histopathological (H&E staining) and immunohistochemical (Ki-67 for cell proliferation and cleaved caspase-3 for apoptosis) analysis was performed on HeLa tumor tissues in mice treated with PBS buffer, Dox-loaded HSH in the absence of $\vec{B}$, free Dox and Dox-loaded HSH in the presence of $\vec{B}$, respectively (D). Scale bar, 50 μm.

vibrates the supramolecular network and triggers the release of encapsulated ICG (Figure 5B).

Temperature at the tumor site treated with or without $\vec{B}$ was detected by an infrared camera. As shown in the lower panel in Figure 5A, temperature around the injection site in tumor was significantly elevated with extended exposure to the magnetic pulses, and the final value reached 62.5 °C after irradiation under $\vec{B}$ for 8 min. In the absence of $\vec{B}$, however, temperature remained constant around 29 °C, confirming that the thermal effect is attributed to the response of HSH to external magnetic stimulus (Figure 5B, lower panel). The thermal effect of HSH under $\vec{B}$ irradiation may also help ICG to diffusely infiltrate surrounding tumor tissue.[47] Furthermore, mice injected with a buffer solution of ICG exhibited instant spread of fluorescence within the animal (Figure S2B). These results highlight that the HSH helps retain loaded cargo within the tumor site and delivers it only when desired through an external trigger ($\vec{B}$ in this case), thus maintaining a baseline concentration of the bioactive drug. More importantly, HSH helps to restrict local heating to the tumor site without elevating temperature of the surrounding area, thus effectively minimize possible damage to the surrounding tissues (Figure 5A lower panel). This is likely due to the formation of a highly viscous and rigid gel once HSH is injected *in vivo*, which stays intact and contains the thermal source, *i.e.*, γ-Fe_2O_3 nanoparticles within the polymeric network (Figure S2A).

The efficiency of HSH in combining thermo-chemotherapy upon $\vec{B}$ stimulus then evaluated in nude mice bearing HeLa tumor. Dox-loaded HSH ([Dox] = 1 mg/mL) was injected into the tumor site on the rear right flank of the mice and tumor volumes were examined for 14 days after treatment. Magnetic-field pulses (2 min each time) were applied every other day, *e.g.*, in group 0, no $\vec{B}$ was applied; in group 1, $\vec{B}$ was applied once on day 2; in group 2, $\vec{B}$ was applied once on day 2 and another time on day 4, *etc.* Consistent with previous assumptions, measurements of tumor volume revealed that *in situ* injection of the HSH on day 0 followed by magnetic-field treatment led to a statistical difference in tumor size (Figure 6A). While mice subjected to $\vec{B}$ for 1 and 2 times yielded tumours that were smaller in size than those in group 0, where mice were treated in the absence of magnetic pulses, only irradiation under $\vec{B} > 3$ times led to a significant reduction in tumor size. Also the tumor volume decreased with extended exposure to $\vec{B}$ (from 1 to 6 doses). The results suggest that the simultaneous release of loaded drug and thermal energy from the injected HSH to the surrounding tumor tissue under $\vec{B}$ plays a crucial role in its antitumor activity, since the tumor size in treatment groups with different exposure doses to the intermittent pulses of magnetic field shows entirely different therapeutic outcomes.

In order to evaluate the potential toxicity of HSH as a therapeutic substrate, body weight of the tumor-bearing mice was also analyzed (Figure 6B). Whereas mice treated in the absence of $\vec{B}$ in group 0 lost 12.5% weight over a period of 14 days, mice subjected to 1 (group 1) or 2 (group 2) doses of magnetic pulse showed less extreme loss, indicating that tumor growth has a significant influence on the body weight of the animals. In contrast, mice treated with multiple intermittent $\vec{B}$ started to gain weight four days after the injection of the HSH, resulting in an average increase of 10.9%, 13.0%, 13.5% and 14.0% from their baseline weights in groups 3, 4, 5 and 6, respectively. At the end of the two-week study, mice were euthanized and the tumors were excised to analyze. As shown in Figure 6C, tumors within mice that had received a combination of magnetic field and Dox-laden HSH showed a more pronounced reduction in size with increased doses of $\vec{B}$ irradiation (from group 1 to group 6). Tumors retrieved from mice that had been injected with Dox-laden HSH but not exposed to any magnetic field (group 0), however, were significantly larger in size.

Hematoxylin and eosin (H&E) staining and immunohis-

tochemical examinations were performed to reveal the antitumor efficiency of HSH. Two weeks after the subcutaneous injection of HeLa cells, the mice were allocated randomly to the following groups and treated with the corresponding conditions: (1) PBS buffer, (2) Dox-loaded HSH in the absence of $\vec{B}$, (3) free Dox and (4) Dox-loaded HSH in the presence of $\vec{B}$. Concentration of Dox in the injected materials was kept constant as 1 mg/mL in group (2), (3) and (4), and 100 μL of the corresponding materials was injected in each mouse in all four groups. While mice in group (1), (2) and (3) were treated in the absence of $\vec{B}$, mice in group (4) were irradiated under magnetic field for 2 min on days 2, 4, 6, 8, 10 and 12. As shown in Figure 6D, tumors were explanted from the euthanized mice after 14 days and H&E staining revealed a decreased number of cancer cells and increased pyknosis in the order of PBS = Dox-loaded HSH > Dox > Dox-loaded HSH under $\vec{B}$, suggesting thermo- and chemotherapeutic modalities acting synergistically.

The expression of Ki-67 and cleaved caspase-3, biomarkers for cell proliferation and apoptosis respectively, were also examined. In comparison to the PBS group, Dox-loaded HSH in the absence of $\vec{B}$ exhibited similar expression of both Ki-67 and cleaved caspase-3, suggesting negligible inhibition of cell proliferation or acceleration of apoptosis, thus confirming good *in vivo* biocompatibility of HSH as an injectable material. On the contrary, Dox-loaded HSH in the presence of $\vec{B}$ irradiation showed more significant inhibition of cell proliferation as denoted by fewer Ki-67 positive cells and increased apoptosis as indicated by more caspase-3 positive cells than free Dox. On the other hand, no noticeable signs of damage or inflammatory lesions were observed in the major organs collected at the end of the study (Figure S3, Supporting Information). The results suggest that a single injection of drug-loaded HSH followed by intermittent $\vec{B}$ irradiation provides an efficient method to suppress tumors *in vivo* by releasing therapeutic drugs and thermal energy to the surrounding tumor tissues in a sustained and controlled manner.

Conclusions

In summary, we have demonstrated the ability of CB[7] to assemble a non-covalent hybrid hydrogel consisting of magnetic nanoparticles in a polymer matrix through supramolecular interactions. A facile self-assembly pathway was designed instead of complicated synthesis based on the molecular-recognition properties and electrostatic interactions of CB[7], leaving the chemical structure and physical properties of γ-Fe_2O_3 nanoparticles intact. Owing to the non-covalent internal interactions and hierarchical structure of the integrated system, drug delivery is only accelerated in the presence of an external magnetic field. The delivery profile is controlled by vibration-accelerated release as well as temperature-facilitated diffusion, endowing the material with both thermo- and chemotherapeutic modalities which are demonstrated both *in vitro* and *in vivo*. With both molecular recognition and supramolecular interactions readily combined within a single system, this manuscript represents a powerful and facile strategy for the construction of stimuli-responsive materials for novel biomedical applications.

Materials and Methods

CB[7] was prepared according to literature procedures.[23,48] Iron(III) precursor $FeCl_3 \cdot 6H_2O$, iron(II) precursor $FeCl_2 \cdot 4H_2O$, CS (deacetylation $\geq$ 95%, viscosity 100-200 mps·s), 1-hydroxybenzotriazole hydrate (HOBT), 3,4-dihydroxyhydrocinnamic acid, N-ethyl-N'-(3-dimethylaminopropyl)carbodiimide hydrochloride (EDC) and Dox were purchased from Energy Chemical. Annexin V Apoptosis Detection Kit FITC was purchased from Sangon Biotech (Shanghai, China), and Calcein-AM/PI Double Stain Kit was from Yeasen (Shanghai, China). All other materials were purchased from Aladdin Reagent Company and used as received.

^{1}H NMR (500 MHz) spectra were recorded using a Bruker Avance AV-500. Chemical shifts were recorded in ppm in D_2O with the internal reference set to 4.79 ppm. UV-vis studies were performed on a UV-2550 SHIMADZU spectrophotometer. Remote controlled heating of the hydrogel nanocomposites was conducted under an alternating electromagnetic field (SPG-10AB-II, Shenzhen Shuangping Power Supply Technologies Company Ltd.) with a power of 300 kHz and 25 kA·m^{-1}. Sample temperature was determined by an infrared camera (E40, FLIR). The hydrodynamic diameter D_h and zeta potential of particles were determined using a Malvern Zetasizer NS90 instrument fitted with a He-Ne laser (λ = 663 nm) at 25 °C. D_h was calculated according to the Stokes-Einstein equation. Zeta potential of the particles was estimated from the electrophoretic mobility according to the Helmholtz-Smoluchowski equation. Dynamic light scattering (DLS) measurements were carried out in triplicate on three independent samples to give an average value.

Rheological characterisation was conducted using a DHR-2 controlled stress rheometer (TA Instruments) fitted with a Peltier stage. All measurements were performed using a 40 mm parallel plate geometry with a gap of 500 μm and analyzed using TA Instruments TRIOS software. A pre-shear of 1 s^{-1} was applied for 60 s prior to further measurement in order to remove loading effects. All measurements presented in this work are reproducible. Dialysis of the functional chitosan was carried out by placing the reaction solutions into a dialysis tube (standard grade regenerated cellulose dialysis membrane, molecular weight cut-off 3500 Da) which was subsequently submerged in specified solvents. The external solutions were stirred at room temperature and replaced with fresh solvents periodically over a 72 h time period (ca. 4-5 times daily). The dialysed polymer solution was then transferred into a round-bottom flask, frozen with liquid nitrogen, and lyophilized on a Scientz-10N bench top freeze drier to yield fluffy solid materials.

Isothermal titration experiments (ITC) were carried out using a NanoITC (TA Instruments) under the following conditions: 25 °C temperature, 1000 rpm stirring speed, 60 s initial delay, and 18 consecutive injections of 10 μL each (the first injection was 0.4 μL) into the cell (950 μL). CAT-CS (1 mM) and CB[7] (0.1 mM) were

dissolved in PBS at pH 7.4 and degassed for 15 min prior to measurements. Heat of dilution was determined by titrating the solution of CAT-CS into water. All the titrations were repeated three times and the blank (CAT-CS in water) subtracted. Data were analyzed by NanoAnalyse software with the "independent sites" model and the first data point was removed from the data set prior to curve fitting. Intravital imaging was conducted on an IVIS Spectrum *in vivo* imaging system (PerkinElmer) with a heated stage and an inhaled isoflurane manifold. Flow cytometry was performed on a BD Accuri C6 instrument. Fluorescence imaging was performed on a Leica DMi8 inverted microscope.

Synthesis of CAT-CS. Catechol-functionalized chitosan was synthesized *via* post-functionalization of CS. To a solution of CS (1.00 g) in water (50 ml) was added HOBT (1.90 g, 12.4 mmol) and the mixture was stirred for 1 h at ambient temperature. 3,4-Dihydroxyhydrocinnamic acid (0.56 g, 3.1 mmol) and EDC (2.38 g, 12.4 mmol) were dissolved in ethanol (15 ml) and added to the solution. After stirring for 3 days, the solution was dialyzed with water and lyophilized to afford a grey powder (1.20 g, 79 %). Typically, ^{1}H-NMR spectrum shows resonances in the region of 6.49-6.73 ppm, which are attributed to the aryl motif of CAT derivatives (see top spectrum in Figure 2A). CAT content was calculated to be 20% by integrating CS and CAT signals, respectively.

Preparation of γ-Fe_2O_3 nanoparticles. Iron(III) precursor ($FeCl_3 \cdot 6H_2O$, 0.32 mol) and iron(II) precursor ($FeCl_2 \cdot 4H_2O$, 0.16 mol) were dissolved in 3.5 L water, and 300 mL of ammonium hydroxide solution (NH_4OH, 8.6 M) was added at room temperature, resulting in the mixture turning black immediately. After 15 min, the nanoparticles were collected with a permanent neodymium magnet and the supernatant was discarded, yielding 30 g of Fe_3O_4 nanoparticles.

The nanoparticles were then suspended in 400 mL of nitric acid (2 M) and stirred for 15 min. After collection of the nanoparticles by removing the supernatant, 600 mL of ferric nitrate solution (0.33 M) was added and the solution was stirred at 90 °C for 30 min. Then the nanoparticles were peptized with 400 mL of nitric acid (2 M) for 15 min at room temperature, then rinsed with acetone (200 mL) for 5 times. The obtained γ-Fe_2O_3 nanoparticles were dispersed in 500 mL of de-ionized water with a concentration of 61.5 g L^{-1}. The pH value of the suspension was tuned to ca. 4.0 for storage.[49] The nanoparticles were collected and re-dispersed in PBS buffer (pH 7.4, 10 mM) for DLS measurements.

Preparation of HSH. Typical HSH was prepared by dissolving CAT-CS (200 mg) in HCl solution (0.1 M, 9 ml) and stirring overnight. To the resulting homogeneous dispersion was added β-glycerophosphate disodium salt (GP, 560 mg) in water (1 ml) dropwise to obtain a solution with pH of 7.15. CB[7] (232 mg, 0.2 mmol, 1 eq. to CAT functional groups) was added and the solution was ultrasonicated for 1 h to facilitate the formation of CAT⊂CB[7]-CS complexes. Subsequently, γ-Fe_2O_3 nanoparticles (10 mg, 0.1 wt% unless stated otherwise) were added to the solution and sonicated for 24 h.

In vitro drug release. Drug release behavior of the HSH in the presence or absence of $\vec{B}$ was evaluated in HeLa cell line. Dox-loaded HSH (disc diameter 12.5 mm, height 5 mm, [Dox] = 30 μM) was placed in complete growth medium (3 ml) and the sample was exposed to $\vec{B}$ for different length of time. HeLa cells were seeded at 1.2×10^5 cells per ml in a polystyrene 12-well plate for 24 h. The cell culture medium was then discarded and replaced by the medium which was used to soak the HSH. The well plate was placed in the incubator for another 24 h before testing.

In vitro thermal therapy. The HSH discs (12.5 mm diameter, 5 mm height) in quartz vials were placed in the centre of the solenoid coil and exposed to $\vec{B}$. Thermal images and data were acquired using an infrared camera, which recorded the surface temperature of the sample. Thermal therapy properties of the HSH upon $\vec{B}$ irradiation were evaluated using HeLa cells. Cells were seeded in 35 mm Petri dishes at 1.2×10^5 cells per ml and cultured in complete growth medium for 24 h. The HSH was cut into discs (35 mm diameter) and wrapped in cling film to prevent water loss. Growth medium was removed from the culture dish, which was then placed directly on top of the HSH in the center of the solenoid coil for heat treatment. The gel and cells were exposed to $\vec{B}$ (300 kHz and 25 $kA \cdot m^{-1}$) for different length of time, and the cells were cultured in complete medium for 24 h before testing in order to allow enough time for a cellular response.

Xenograft tumor studies. Tumors were created by injecting 10^6 HeLa cells (American Type Cell Culture) in 80 μL PBS buffer into the rear right flank of six to eight-week-old nude mice. Following two weeks of tumor inoculation, mice used for the study were normalized for tumor size by selecting mice with tumor volume between 170 and 190 mm^2. These mice were randomly distributed in different treatment groups. Drug-loaded HSH ([Dox] = 1 mg/mL, 100 μL) was injected directly into tumor tissues. Magnetic-field treatments were applied for 2 min every other day and the overall treatment time was listed in Figure 6A and B. In all treatment groups, mice were injected with HSH on day 0. In group 0, mice were not treated with $\vec{B}$; in group 1, mice were treated with $\vec{B}$ for 2 min on day 2; in group 2, mice were treated with $\vec{B}$ for 2 min on day 2 and 4; in group 3, mice were treated with $\vec{B}$ for 2 min on day 2, 4 and 6; in group 4, mice were treated with $\vec{B}$ for 2 min on day 2, 4, 6 and 8; in group 5, mice were treated with $\vec{B}$ for 2 min on day 2, 4, 6, 8 and 10; in group 6, mice were treated with $\vec{B}$ for 2 min on day 2, 4, 6, 8, 10 and 12.

References

[1] L. R. Hirsch, R. J. Stafford, J. A. Bankson, S. R. Sershen, B. Rivera, R. E. Price, J. D. Hazle, N. J. Halas, J. L. West, *Proc. Natl. Acad. Sci.* **2003**, *100*, 13549–13554.

[2] D. O'Neal, L. R. Hirsch, N. J. Halas, J. Payne, J. L. West, *Cancer Lett.* **2004**, *209*, 171–176.

[3] X. Zhu, J. Li, X. Qiu, Y. Liu, W. Feng, F. Li, *Nat. Commun.* **2018**, *9*, 2176.

[4] P. Chakravarty, R. Marches, N. S. Zimmerman, A. D.-E. Swafford, P. Bajaj, I. H. Musselman, P. Pantano, R. K. Draper, E. S. Vitetta, *Proc. Natl. Acad. Sci.* **2008**, *105*, 8697–8702.

[5] R. Lencioni, L. Crocetti, P. Petruzzi, C. Vignali, E. Bozzi, C. Della Pina, I. Bargellini, D. Cioni, F. Oliveri, P. De Simone, C. Bartolozzi, M. Brunetto, F. Filipponi, *J. Hepatol.* **2018**, *49*, 217–222.

[6] M. Johannsen, B. Thiesen, P. Wust, A. Jordan, *Int. J. Hyperthermia* **2010**, *26*, 790–795.

[7] H. Yan, W. Shang, X. Sun, L. Zhao, J. Wang, Z. Xiong, J. Yuan, R. Zhang, Q. Huang, K. Wang, B. Li, J. Tian, F. Kang, S.-S. Feng, *Adv. Funct. Mater.* **2018**, *28*, 1705710.

[8] S. He, H. Zhang, Y. Liu, F. Sun, X. Yu, X. Li, L. Zhang, L. Wang, K. Mao, G. Wang, Y. Lin, Z. Han, R. Sabirianov, H. Zeng, *Small* **2018**, *14*, 1870133.

[9] R. K. Gilchrist, R. Medal, W. D. Shorey, R. C. Hanselman, J. C. Parrott, C. B. Taylor, *Annals of Surgery* **1957**, *146*, 596–606.

[10] K. F. Chu, D. E. Dupuy, *Nat. Rev. Cancer* **2014**, *14*, 199.

[11] X. Yao, X. Niu, K. Ma, P. Huang, J. Grothe, S. Kaskel, Y. Zhu, *Small* **2017**, *13*, 1602225.

[12] L. Wang, N. J. Long, L. Li, Y. Lu, M. Li, J. Cao, Y. Zhang, Q. Zhang, S. Xu, Z. Yang, C. Mao, M. Peng, *Light-Sci. Appl.* **2018**, *7*, 1.

[13] P. R. Austin, C. J. Brine, J. E. Castle, J. P. Zikakis, *Science* **1981**, *212*, 749–753.

[14] F.-Y. Hsieh, L. Tao, Y. Wei, S.-h. Hsu, *Npg Asia Mater.* **2017**, *9*, e363.

[15] H. Wang, S. Mukherjee, J. Yi, P. Banerjee, Q. Chen, S. Zhou, *ACS Appl. Mater. Interfaces* **2017**, *9*, 18639–18649.

[16] L. Song, L. Li, T. He, N. Wang, S. Yang, X. Yang, Y. Zeng, W. Zhang, L. Yang, Q. Wu, C. Gong, *Sci. Rep.* **2016**, *6*, 37600.

[17] F.-Y. Hsieh, H.-W. Han, X.-R. Chen, C.-S. Yang, Y. Wei, S.-h. Hsu, *Biomaterials* **2018**, *174*, 31–40.

[18] G. Shi, W. Chen, Y. Zhang, X. Dai, X. Zhang, Z. Wu, *Langmuir* **2018**, DOI 10.1021/acs.langmuir.8b01834.

[19] G. Gao, Y.-W. Jiang, H.-R. Jia, F.-G. Wu, *Biomaterials* **2018**, DOI https://doi.org/10.1016/j.biomaterials.2018.09.045.

[20] J. Liu, C. S. Y. Tan, Z. Yu, N. Li, C. Abell, O. A. Scherman, *Adv. Mater.* **2017**, *29*, 1605325.

[21] S. Liu, C. Ruspic, P. Mukhopadhyay, S. Chakrabarti, P. Y. Zavalij, L. Isaacs, *J. Am. Chem. Soc.* **2005**, *127*, 15959–15967.

[22] J. Liu, Y. Lan, Z. Y. Yu, C. S. Y. Tan, R. M. Parker, C. Abell, O. A. Scherman, *Acc. Chem. Res.* **2017**, *50*, 208–217.

[23] J. Kim, I.-S. Jung, S.-Y. Kim, E. Lee, J.-K. Kang, S. Sakamoto, K. Yamaguchi, K. Kim, *J. Am. Chem. Soc.* **2000**, *122*, 540–541.

[24] X.-M. Chen, Y. Chen, Q. Yu, B.-H. Gu, Y. Liu, *Angew. Chem. Int. Ed.* **2018**, *57*, 12519–12523.

[25] X. Du, J. Zhou, J. Shi, B. Xu, *Chem. Rev.* **2015**, *115*, 13165–13307.

[26] I. Hwang, W. Jeon, H. Kim, D. Kim, H. Kim, N. Selvapalam, N. Fujita, S. Shinkai, K. Kim, *Angew. Chem. Int. Ed.* **2006**, *46*, 210–213.

[27] R. W. Taylor, T.-C. Lee, O. A. Scherman, R. Esteban, J. Aizpurua, F. M. Huang, J. J. Baumberg, S. Mahajan, *ACS Nano* **2011**, *5*, 3878–3887.

[28] Q.-L. Li, Y. Sun, Y.-L. Sun, J. Wen, Y. Zhou, Q.-M. Bing, L. D. Isaacs, Y. Jin, H. Gao, Y.-W. Yang, *Chem. Mater.* **2014**, *26*, 6418–6431.

[29] I. Hwang, K. Baek, M. Jung, Y. Kim, K. M. Park, D.-W. Lee, N. Selvapalam, K. Kim, *J. Am. Chem. Soc.* **2007**, *129*, 4170–4171.

[30] H. Chen, S. Hou, H. Ma, X. Li, Y. Tan, *Sci. Rep.* **2016**, *6*, 20722.

[31] N. Hüsken, R. W. Taylor, D. Zigah, J.-C. Taveau, O. Lambert, O. A. Scherman, J. J. Baumberg, A. Kuhn, *Nano Lett.* **2013**, *13*, 6016–6022.

[32] J. H. Ryu, Y. Lee, W. H. Kong, T. G. Kim, T. G. Park, H. Lee, *Biomacromolecules* **2011**, *12*, 2653–2659.

[33] S. J. Barrow, S. Kasera, M. J. Rowland, J. del Barrio, O. A. Scherman, *Chem. Rev.* **2015**, *115*, 12320–12406.

[34] S. Kasera, L. O. Herrmann, J. d. Barrio, J. J. Baumberg, O. A. Scherman, *Sci. Rep.* **2014**, *4*, 6785.

[35] F. Benyettou, H. Fahs, R. Elkharrag, R. A. Bilbeisi, B. Asma, R. Rezgui, L. Motte, M. Magzoub, J. Brandel, J. C. Olsen, F. Piano, K. C. Gunsalus, C. Platas-Iglesias, A. Trabolsi, *RSC Adv.* **2017**, *7*, 23827–23834.

[36] Y. Wu, D. U. Shah, C. Liu, Z. Yu, J. Liu, X. Ren, M. J. Rowland, C. Abell, M. H. Ramage, O. A. Scherman, *Proc. Natl. Acad. Sci.* **2017**, *114*, 8163–8168.

[37] A. Vashist, A. Vashist, Y. K. Gupta, S. Ahmad, *J. Mater. Chem. B* **2014**, *2*, 147–166.

[38] Z. Tu, H. Qiao, Y. Yan, G. Guday, W. Chen, M. Adeli, R. Haag, *Angew. Chem. Int. Ed.* **2018**, *57*, 11198–11202.

[39] M. N. R. Kumar, *React. Funct. Polym.* **2000**, *46*, 1–27.

[40] Y.-F. Ding, S. Li, L. Liang, Q. Huang, L. Yuwen, W. Yang, R. Wang, L.-H. Wang, *ACS Appl. Mater. Interfaces* **2018**, *10*, 9980–9987.

[41] P. Manivasagan, N. Quang Bui, S. Bharathiraja, M. Santha Moorthy, Y.-O. Oh, K. Song, H. Seo, M. Yoon, J. Oh, *Sci. Rep.* **2017**, *7*, 43593.

[42] H.-Y. Chiu, Y.-G. Tsay, S.-C. Hung, *Sci. Rep.* **2017**, *7*, 10113.

[43] M. Liu, X. Zeng, C. Ma, H. Yi, Z. Ali, X. Mou, S. Li, Y. Deng, N. He, *Bone Res.* **2017**, *5*, 17014.

[44] A. Chenite, C. Chaput, D. Wang, C. Combes, M. Buschmann, C. Hoemann, J. Leroux, B. Atkinson, F. Binette, A. Selmani, *Biomaterials* **2000**, *21*, 2155–2161.

[45] W. Li, J. Wang, J. Ren, X. Qu, *Chem. Sci.* **2015**, *6*, 6762–6768.

[46] W. Li, K. Dong, J. Ren, X. Qu, *Angew. Chem. Int. Ed.* **2016**, *55*, 8049–8053.

[47] Z.-Q. Zhang, S.-C. Song, *Biomaterials* **2017**, *132*, 16–27.

[48] D. Jiao, N. Zhao, O. A. Scherman, *Chem. Commun.* **2010**, *46*, 2007–2009.

[49] R. Massart, *IEEE Trans. Magn.* **1981**, *17*, 1247–1248.

Entry for the Table of Contents (Please choose one layout only)

Layout 1:

Supramolecular Self-Assembly

*Haishi Qiao, Jing Jia, Wei Chen, Bin Di, Oren A. Scherman, Chi Hu**

Magnetic Regulation of Thermo-Chemotherapy from a Cucurbit[7]uril-Crosslinked Hybrid Hydrogel

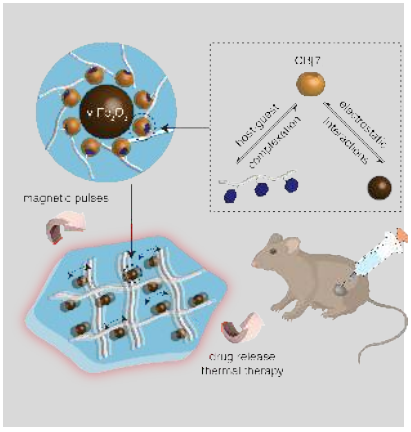

Cucurbit[7]uril-mediated magnetic hydrogel: The fabrication, characterization and therapy efficiency of a noncovalent-bonded hydrogel network, which is assembled by utilizing cucurbit[7]uril as a supramolecular linker to "stick" superparamagnetic γ-Fe_2O_3 nanoparticles onto the polymer backbone of catechol-functionalized chitosan are described. The unique barrel-shaped structure of cucurbit[7]uril not only facilitates host-guest recognition with the catechol derivatives, but also forms robust electrostatic interactions between its carbonyl portals and the γ-Fe_2O_3 nanoparticles in a supramolecular manner which leaves the physical and chemical properties of the nanoparticles intact. The γ-Fe_2O_3 nanoparticles display vibrational movement and heat generation under alternating magnetic field, endowing the formed hybrid supramolecular hydrogel with both thermo- and chemotherapy modalities, which are demonstrated both *in vitro* and *in vivo*. This work introduces a facile strategy to construct non-covalent interactions between a polymer matrix and the incorporated nanoparticles, which is amendable to a wide range of biomedical and industrial applications.

Layout 2:

Catch Phrase:

*Author(s), Corresponding Author(s)**

. . . . . *Page Page*

Title Text

((The TOC Graphic should not exceed the size of this area))

Text for Table of Contents, max. 450 characters.